Squeeze flow between a sphere and a textured wall

T. Chastel, Anne Mongruel

Squeeze flow between a sphere and a textured wall

T. Chastel and A. Mongruel[1, a)]

Physique et Mécanique des Milieux Hétérogènes

UMR 7636 CNRS - ESPCI - Université Pierre et Marie Curie - Université Paris-Diderot

10 rue Vauquelin, 75231 Paris cedex 05, France

The motion of a millimetric sphere, translating in a viscous fluid towards a wettable textured wall, is investigated experimentally. The textures consist of square arrays of cylindrical or square micro-pillars, the height, width and spacing of which are varied, keeping the periodicity small compared to the sphere radius. An interferometric device is used to measure the sphere vertical displacement, for distances between the sphere and the base of the pillars smaller than 0.1 sphere radius, and with a resolution of 200 nm. At a given distance from the top of the pillars, the sphere velocity is found to be significantly larger than the corresponding velocity for a smooth solid wall. A squeeze flow model of two adjacent fluid layers is developed in the lubrication approximation, one fluid layer having an effective viscosity that reflects the viscous dissipation through the array of pillars. The pressure field in the gap between the sphere and the textured surface is then used to obtain the drag force on the sphere and hence its velocity. Adjustment of the model to the velocity measurements yields the effective viscosity for a given texture. Finally, a correlation between the effective viscosity and the geometry of the pillar array is proposed.

Keywords: squeeze flow, textured wall, lubrication approximation

---

[a)]Electronic mail: anne.mongruel@upmc.fr

I.   INTRODUCTION

When a spherical particle moves towards a planar smooth boundary in a viscous fluid lubrication theory predicts that the force resisting the approach diverges as the gap between the particle and the wall vanishes[1,2]. In practice, this divergence is regularized when the interacting surfaces are rough[3,4]. This physical importance of roughness is crucial to the field of concentrated suspensions dynamics. As a matter of fact, surface roughness, naturally present on most surfaces, has a strong effect on the short-range interaction between a pair of particles, reducing the lubrication interaction, and allowing for solid-solid contacts[5].

Here we consider a smooth sphere approaching a wall with controlled roughness. This model situation is used to understand the modification of the hydrodynamic interactions at close distance between particles, or between particles and walls, brought by surface roughness. A specific wall texture has been designed using arrays of micro-pillars. The drag force on the sphere is a result of the pressure field developing in the thin viscous fluid layer that is squeezed out of the gap between the textured wall and an approaching sphere. We remark and stress that the drag force is measured as a function of the gap between the sphere and the top surface of the textures. As a consequence, the hydrodynamic resistance is decreased relative to a no-slip boundary condition imposed by a plain smooth wall at the top surface of the micro-pillar array. Alternatively, the reduced drag can be interpreted as due to the permeation of the fluid through the micro-pillar array, similarly to the case of a sphere approaching a permeable wall[6]. The reduction of hydrodynamic force on a sphere approaching, at controlled velocity, micro-textured surfaces wetted by water in the Wenzel regime, has been measured using a dynamic surface force apparatus[7] (SFA) , and an atomic force microscope[8] (AFM) . Similar effects have been obtained for a rough sphere[9] or a textured cylindrical surface[10] approaching a smooth plane wall .

In our experiments, we measure the velocity of a sphere driven by a constant gravitational force towards a textured surface. The sphere is smooth, millimetric, and settles in a very viscous oil. The textured surface consists of a plane wall decorated with a square array of micro-pillars and is completely wetted by the oil. The periodicity of the array, L, is very small compared to the sphere radius, a. The displacement of the sphere is measured by laser interferometry, with a resolution of 0.2 μm. We focus on the near-wall region, where the value of the gap between the sphere and the top of the texture, h_0, is much smaller than the

sphere radius. At a given distance from the top of the pillars, the sphere velocity is measured to be larger than the corresponding velocity for a smooth wall. Such a velocity enhancement was first found with the same interferometric device near a wall with periodic corrugations[4]. It was also obtained near surfaces with random roughness[11], and near textured walls with microgrooves[12]. The results were interpreted using the notion of an equivalent smooth plane that is shifted down from the top of the corrugations. It was established theoretically that the shift length is the average of two effective slip lengths, calculated by averaging the shear flow over the wavelength of the corrugations in the two directions parallel and perpendicular to the corrugations[4,13]. Thus, the equivalent plane boundary approach is only valid in the far-field region, where the gap, h_0, is one order of magnitude larger than the wavelength of the corrugations, L, as observed experimentally[4].

Here, we propose an alternative model to the equivalent plane boundary, in order to interpret the observed enhancement of sphere velocity in the near-field region, $h \ll L$. The specificity of our model is to replace the composite medium (flow + pillars) by a continuous medium with an effective viscosity reflecting the viscous dissipation by the array of the pillars. This idea has been recently introduced in the context of coating flow[14]. In our model, the sphere is embedded in one fluid, and approaches a plane surface covered with a layer of a second fluid, of constant thickness and of larger viscosity than the first one. The lubrication approximation is used to derive the flow in the two fluid layers, as the sphere approaches the surface at distances much smaller than the particle radius. From the calculated pressure field, the drag force on the sphere approaching the surface is finally obtained.

The paper is organized as follows. In section II, the experimental device is described together with the geometry of the textures, and the enhancement of velocity for a sphere approaching a micro-pillar array is measured. In section III, the squeeze flow model is formulated for two adjacent fluid layers, and the pressure field and resulting drag force on the sphere are obtained. The calculated velocity of the sphere is compared to experimental data, yielding the value of the effective viscosity of the second fluid. In section IV, the results for the effective viscosity are discussed in terms of viscous dissipation through an array of pillars. The effective viscosity is correlated to the geometry of the pillar array. Finally, section V presents a brief conclusion.
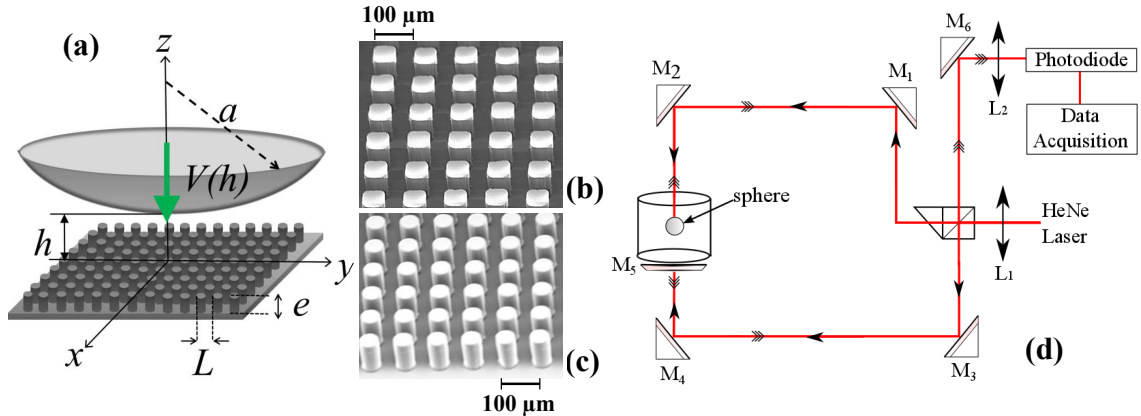
FIG. 1. (a) Sketch of a sphere approaching a wall decorated with an array of micro-pillars. SEM photograph of micropillars arrays obtained by photolithography : (b) square pillars ($e = 90$ μm, $L = 97$ μm, $2b = 53$ μm) and (c) cylindrical pillars ($e = 92$ μm, $L = 88$ μm, $2b = 48$ μm). (d) Sketch of the interferometer and of the data conversion and acquisition set-up (Mirrors are denoted by M and lenses by L).

II.   MEASUREMENT OF SPHERE MOTION PERPENDICULAR TO A TEXTURED WALL

We use an interferometric technique, first designed to measure very small displacements of a sphere with a resolution on the sphere displacement of 0.2 μm[15]. Recently, this device was used to measure the effect of wall corrugations[4] and micro-grooves[12] on the sphere velocity. In the present study, new type of surfaces, i.e. textured walls with arrays of micro-pillars, are tested for the first time with this device.

A.   Materials and procedures

1.   Interferometry

The sphere is embedded in a fluid contained in a cylindrical vessel with a 50 mm diameter and a 40 mm height. The lateral walls are made with altuglass, and the top and bottom plane walls are made of glass of optical quality. The fluid is a Newtonian and incompressible PDMS (silicone) oil, with density of $\rho_f = 978$ kg m^{-3} and kinematic viscosity $\nu = 0.1$ m^{2}s^{-1} at 25°C. Experiments are conducted at ambient room temperature. Physical properties of
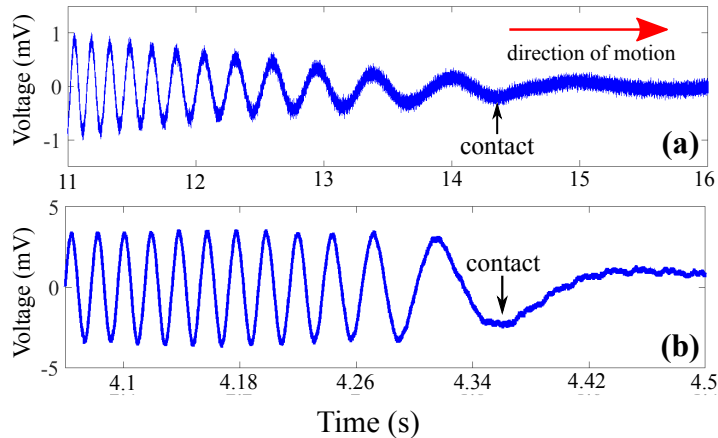
FIG. 2. Examples of interferometric signal for the motion of a sphere approaching (a) a quasi-smooth wall (glass) and (b) an array of micropillars. Between two maxima of the signal, the sphere has moved a distance equal to $\lambda/2n = 0.224\,\mu$m.

the oil (viscosity, refraction index) vary slowly with temperature. The oil has a Newtonian behavior for shear rates up to $100\,\mathrm{s}^{-1}$. The particles are spherical steel balls with density $\rho_p = 7.8 \times 10^3\,\mathrm{kg\,m^{-3}}$ and diameters ranging from $7\,\mathrm{mm}$ to $12.7\,\mathrm{mm}$. The roughness, R_a, of the steel balls, as indicated by the manufacturer, is $0.013\;\mu$m. The Reynolds number based on particle diameter and particle Stokes velocity, $Re = (2a)V_{St}/\nu$, is vanishingly small ($Re \simeq 10^{-5}$).

The vessel is inserted in the interferometric device so that the sphere reflects one of the laser beam, whereas the second beam is reflected by a fixed mirror at the bottom of the wall. Interference fringes (circular rings) are formed, that move according to the sphere displacement. The recorded signal is the light intensity at the centre of the interference pattern. Signal variation from one maximum (bright fringe) to another is due to a displacement of the sphere equal to $\lambda/2n$, where λ is the wavelength of the laser, and n the index of refraction of the suspending fluid. Here, with a silicon oil ($n = 1.404$) and a He-Ne laser beam ($\lambda = 632.8$ nm), we have $\lambda/2n = 0.224\,\mu$m. The sphere velocity is related to the velocity of fringe displacement by multiplying $\lambda/2n$ by the frequency of the signal. The signal, after opto-electronic conversion by a photodiode (Thorlabs DET10A/M), is recorded with an electronic oscilloscope, transferred to a PC and processed by a Matlab code for detecting its extreme values as a function of time. The spatial resolution is therefore equal to $\lambda/2n = 0.224\,\mu$m.

Figure 2(a) depicts the signal evolution for a sphere arriving at a quasi-smooth wall (optical glass). The deceleration of the sphere is reflected in the decrease of the amplitude,

and increase of the period of the signal, until contact occurs. The contact position with the wall ($h_0 = 0$) is defined from the recorded signal, as the time when the period of the signal becomes very large indicating a vanishing velocity. This is done with an error of the order of 224 nm on the contact position. From this contact position, the previous positions of the sphere are reconstructed by multiplying the velocity by the time interval. Note that the signal-to-noise ratio deteriorates at vanishing frequency, because the low frequency limit of the oscilloscope is reached. The error on the frequency of the signal comes from the error on the time at which a maximum is detected. The measured frequency is averaged over 7 to 8 periods (75 points), so that the velocity may appear to be very smooth. The resulting error on the velocity is smaller than 1%. However, no averaging has been applied just before the contact, in order to capture the rapid variations in velocities occurring in that region. Here, the error on the velocity can be estimated not to exceed 5%.

2.   *Textured surfaces*

Textured surfaces with controlled texture geometry were fabricated in clean room using standard lithography. In a first step, geometric shapes are transferred from a mask to a silicone (Si/SiO2) wafer coated with a photo-reticulable (SU8, MicroChem) resin, by exposure to UV, developing and hard-baking. The thickness of the film is controlled by spin coating. The size of the structures obtained in this first step are checked by mechanical profilometry. In a second step, a replica molding of the SU8 structures is obtained by soft lithography, using a thermo-reticulable PDMS (Sylgard 184). In our case, these moldings are not chosen as a final material, because they are likely to swell when in contact with silicone oil. A last step is then to obtain a replica of the PDMS molding by soft imprint of a photo-curable polymer, a thiolene based resin (NOA 81, Norland optical adhesives) on glass microscope slides (to be fixed at the bottom of the vessel). This resin was chosen for its good resistance to compression, and its good adhesion to glass. The final structures are observed by scanning electron microscopy (Figure 1). We checked that these surfaces are oleophilic : a millimetric drop of silicon oil deposited on the surface shows progressive imbibition, until the contact angle reaches an equilibrium value of order 30°. So that we expect that the oil completely fills the space between the pillars, without air bubbles being trapped at the solid/oil interface (Wenzel state).
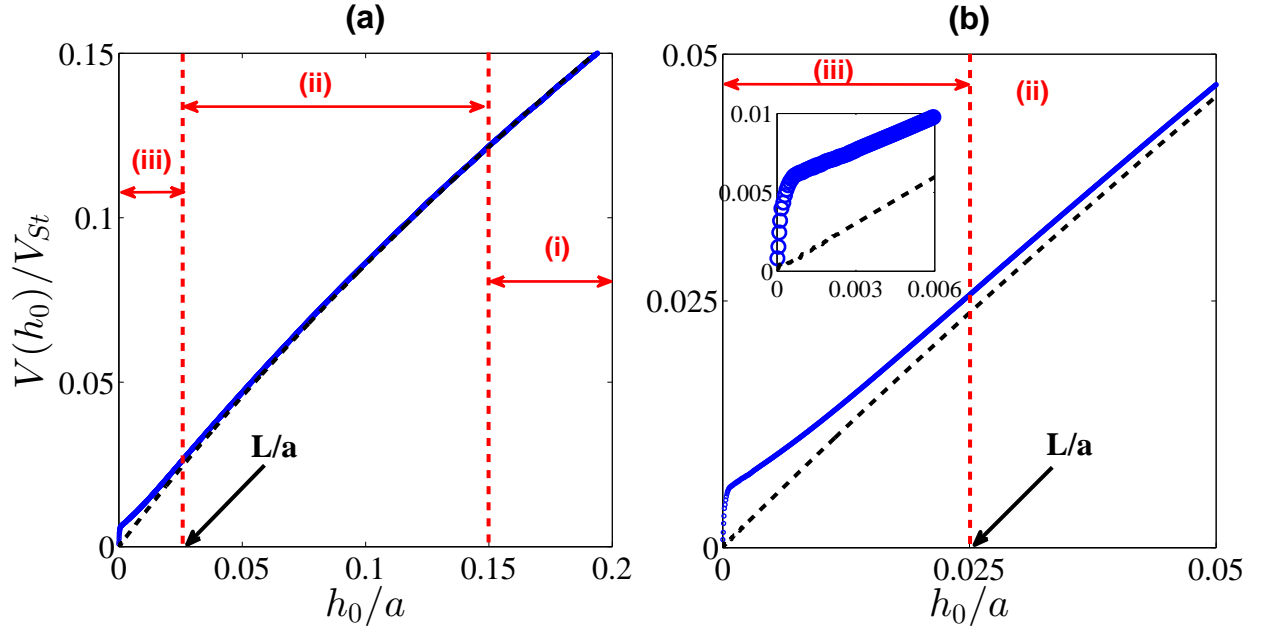
FIG. 3. Sphere dimensionless mobility $V(h_0)/V_{St}$ as a function of dimensionless gap h_0/a, measured near a smooth wall (dashed line) and near an array of cylindric micro-pillars with e = 69 μm, L = 88 μm, 2b = 48 μm (circles). The diameter of the sphere is 2a = 7 mm. (a) Matching of the two curves in region (i). (b) Mobility enhancement due to the textures in region (ii). Insert shows region (iii) with a more pronounced mobility enhancement followed by an abrupt deceleration.

Various texture geometries have been tested in this work. We denote e as the height of the pillars (ranging from 20 to 130 μm), L the wavelength of the array (ranging from 88 to 244 μm), and $2b$ the diameter (side) of cylindrical (square) pillars respectively (ranging from 48 to 106 μm). The area fraction ϕ of the liquid-liquid interface at the top of the textures is $\pi b^2/L^2$ and $4b^2/L^2$ for cylindrical and square pillars arrays respectively, and ranges from 0.05 to 0.45.

B.   Mobility curves

In the limit of small Reynolds number, the drag force F_D on a sphere of radius a moving in a fluid of viscosity μ at a given distance h_0 from a solid wall with a velocity $V(h_0)$ may be written as : $F_D = 6\pi\mu a f(h_0)V(h_0)$. Here, $f(h_0)$ is a dimensionless friction factor, that represents the resistance to motion caused by the hydrodynamic interaction with the wall,

7

and that increases as the distance to the wall decreases. In the case where the interacting surfaces are smooth, this friction factor depends only on the normalized gap $\epsilon_0 = h_0/a$, and $f(\epsilon_0)$ has been calculated as a series[1,2]. This exact solution coincides for $\epsilon_0 < 0.25$ within 1% error with the asymtotic expansion[16] : $f(\epsilon_0) = 1/\epsilon_0 - 1/5 \ln[\epsilon_0] + 0.9713$. It also coincides for $\epsilon_0 < 0.01$ within 1% error with the standard result of lubrication theory[16] : $f_T(\epsilon_0) = 1/\epsilon_0$. In settling experiments, and in the limit of negligible sphere inertia, the drag is balanced by constant gravity forces, also equal to the Stokes drag in an infinite fluid, $F_{St} = 6\pi\mu a V_{St}$, where V_{St} is the Stokes velocity. Thus, the mobility coefficient defined as the ratio of the sphere velocity at a distance h_0 from the wall, to the Stokes velocity, is equal to the inverse of the friction factor :

$$\frac{V(h_0)}{V_{St}} = \frac{1}{f(\epsilon_0)}. \tag{1}$$

1.   General features

In our experiments, the velocity $V(h_0)$ of a sphere approaching a textured wall is measured as a function of gap h_0, the smallest distance between the sphere and the top of the textures (Figure 1). Here, the friction factor becomes, in addition to ϵ_0, a function of the texture geometry. This is illustrated in Figure 3, where the mobility (the inverse of the friction factor) of a sphere of radius $a = 3.5$ mm has been measured close to a textured wall with cylindrical micro-pillars of height $e = 69$ μm, radius $b = 24$ μm, and periodicity $L = 88$ μm. The mobility of the same sphere measured close to a smooth surface is presented also for comparison. Note that in that case, our measurements are perfectly described by the Cox-Brenner asymptotic expansion, and, for $\epsilon_0 < 0.01$, by the lubrication theory $1/f_T = \epsilon_0$. The mobility curve obtained close to a textured wall can be divided into three regions, depending on the spatial scale of observation.

In the region (i), the most far away from the wall, the effect of the textures is negligible and the mobility curve for a smooth surface is recovered. Hence, we have adjusted the value of the Stokes velocity V_{St} so that the velocity matches the curve measured in the same cell for a quasi-smooth (glass) surface, with the same fluid and same sphere diameter (reference curve). In figure 3(a), the matching holds for $\epsilon_0 > 0.15$. Note that with this procedure, the effects of the confinement by the lateral walls can be implicitly taken into account, but we have checked that they remain unimportant up to $\epsilon_0 = 0.3$. The main source of error with

the adjustment procedure comes from the variations of the fluid viscosity with temperature from an experiment to another, but these variations are kept small.

In the far-field region (ii), defined as $(L/a) \leq \epsilon_0 \leq 0.15$, the sphere velocity is significantly influenced by the textures. Here, $L/a = 0.025$. Considering figure 3(b), at a given distance from the top of the textures, the mobility is larger than its value at the same distance from a smooth wall. Moreover, this mobility enhancement is, in that case, a simple shift of the reference curve, in agreement with the equivalent plane boundary model. Here, the shift along the horizontal axes yields an effective slip length of 7 μm.

In the near-field region (iii), defined as $\epsilon_0 \leq (L/a)$, the velocity enhancement is even more significant, and larger than would be predicted by the equivalent plane boundary model (see insert in Figure 3(b)). Finally, for $\epsilon_0 \leq (b/a)$, the sphere decelerates abruptly, within a few interfringes, before it stops completely. This deceleration is also visible on the interferometric signal measured near an array of micro-pillars and shown in Figure 2(b). This corresponds to the interaction of the sphere with the nearest pillar of radius b. Here, $b/a = 0.007$. It is not the purpose of the present work to describe with more precision this part of the mobility curve. In the following, we will focus on the effect of texture geometry in the part of near-field region (iii) limited to $b/a \leq \epsilon_0 \leq L/a$.

2. Effect of texture geometry on the sphere mobility

Figure 4 depicts the sphere mobility measured near arrays of cylindrical micro-pillars of various concentration and height. The diameter of the pillars is essentially the same in all experiments (2b varies between 40 and 50 μm from one array to another).

Figure 4(a) shows the sphere mobility measured for different pillar concentrations, ϕ, at a fixed pillar height ($e = 20$ μm). The mobility is larger near a textured wall than near a smooth wall. Moreover, the smaller the pillar concentration, the higher the mobility enhancement. The effect of the textures is remarkably significant for a small pillar concentration. For example, for $\phi = 0.1$ and $e = 20$ μm, it is found that the mobility at $\epsilon_0 = 0.004$ is increased by a factor of about 2 compared to its value at the same distance from a smooth wall. This is consistent with the idea of the squeezed fluid escaping more easily through less concentrated array of pillars, thus decreasing the pressure in the gap compared to the case of a plain smooth wall, and finally decreasing the drag force on the sphere. For concentrated
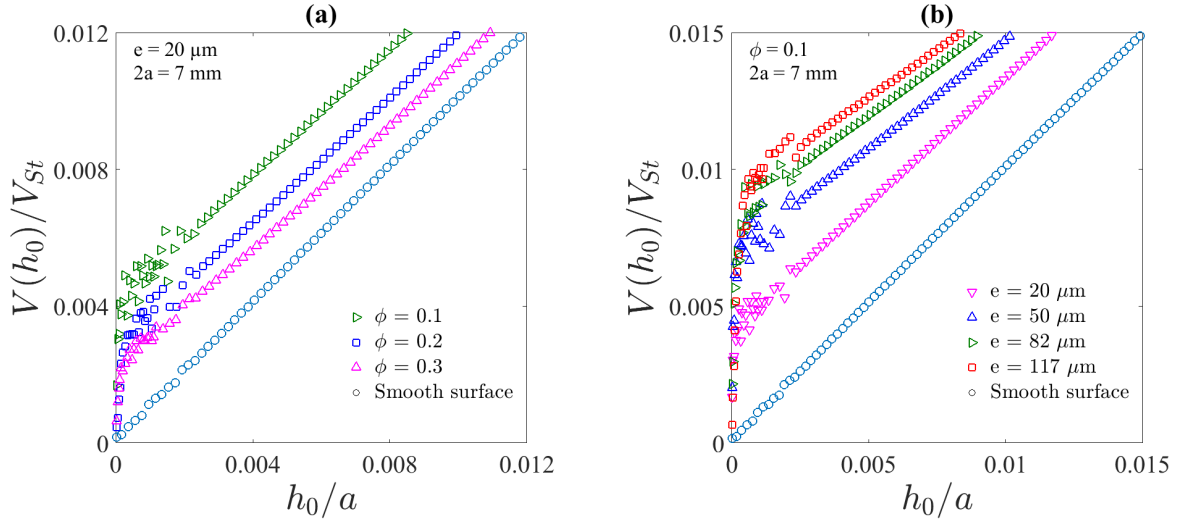
9

FIG. 4. Mobility of a sphere (diameter $2a = 7$ mm) measured near arrays of cylindrical micro-pillars (a) with fixed pillar height, $e = 20$ μm, and different pillar concentrations, $\phi = 0.1$, 0.2 and 0.3. (b) with fixed pillar concentration, $\phi = 0.1$, and different pillar heights, $e = 20$, 50, 82 and 117 μm. Circles : Mobility measured near a smooth surface.

arrays, on the contrary, the mobility approaches the limiting case of a plain smooth wall (which would be recovered for $\phi = 1$).

In Figure 4(b), the pillar height has been varied at a fixed pillar concentration $\phi = 0.1$. In all cases, the mobility enhancement increases with increasing pillar height, e. However, this effect is more efficient when the concentration is the smallest ($\phi = 0.1$). In the limit of vanishing pillar concentration, the drag tends towards the drag measured near a smooth wall. However, measuring the drag from the top of the pillars amounts to shift the velocity curve along the horizontal axis by a distance of the order of the pillar height. Indeed, it can be observed that the different mobility curves are approximately shifted from the reference curve of the smooth wall. However, the equivalence is not conserved for the highest pillars. Rather, a saturation is observed : increasing further the pillars height does not give rise to any supplementary mobility increase. Moreover, the curves are not parallel. This saturation is due to the fact that the motion of the fluid between the pillars is impeded by the proximity of more and more pillars.

Similar trends have been observed for textures made of square pillars, with the same qualitative effects of pillar height and concentration on the sphere mobility, as shown in

Figure 7(b).

III.   LUBRICATED SQUEEZE FLOW OF TWO ADJACENT FLUID LAYERS

In this section, we develop a flow model in the lubrication approximation, for the squeeze flow between a sphere and a wall, of two adjacent immiscible fluid layers of different viscosities. The smooth sphere is immersed in one fluid, and moves towards a smooth wall that is covered with a layer of a second fluid. A strong assumption of this model is that the plane interface between the two fluid layers remains undeformed during the process of squeezing. In practice, this is unlikely to occur as the sphere gets closer to the interface, even if the interface deformation could be impeded by several mechanisms[17] like large density gradients, or large interfacial tension. In our experiments however, the height of the second fluid layer is by definition equal to the height of the pillars, and thus remains uniform and constant during the sphere approach. We consider this layer as a continuous medium having an effective viscosity larger than the viscosity of the actual fluid flowing between the pillars[14]. The configuration is sketched in Figure 5. The sphere moves in the first fluid, denoted "1", that occupies, at a given time t, the region of the space such as $e \leq z \leq h(r)$, with $h(r)$ the equation of the sphere surface. The viscosity of this first fluid layer is $\mu_1 \equiv \mu$. The second fluid, denoted "2", forms a layer of uniform thickness e, and is in contact with the ground and with the top fluid. It thus occupies the portion of the space $0 \leq z \leq e$. The viscosity of this second fluid layer will be denoted as $\mu_2 = k\mu$, with k a dimensionless coefficient larger than unity.

A.   Model formulation

We consider the axisymmetric configuration sketched in Figure 5. The sphere moves in fluid "1" towards fluid "2", and at a given time t, it is situated at a distance h_0 from the top of layer of fluid "2". We denote as V_0 the velocity of the sphere at this distance h_0 (with $V_0 > 0$ corresponding with motion towards fluid "2").

For values of distance h_0 much smaller than the sphere radius a, the equation of the
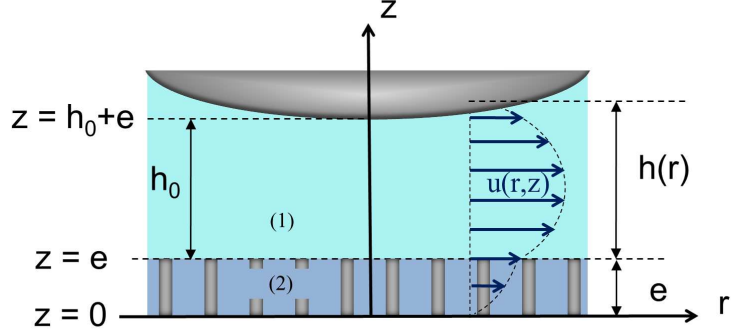
11

FIG. 5. Sketch of the squeeze flow of a two adjacent fluid layers with different viscosities.

sphere surface is approximated by :

$$h(r) = h_0 + \frac{r^2}{2a}. \tag{2}$$

We solve the classical lubrication equations for the axisymmetric velocity field in each fluid layer, valid in the limit $(h_0 + e) \ll a$. The continuity equation implies that $w_i \ll u_i$, with $(u_i(r,z), w_i(r,z))$ being the velocity components in r and z directions of layer number, i. Thus, the equations of motion reduce to :

$$\frac{\partial p_i}{\partial r} = \mu_i \frac{\partial^2 u_i}{\partial z^2}, \quad \frac{\partial p_i}{\partial z} = 0. \tag{3}$$

for each layer, in which μ_i is the dynamic viscosity of layer number, i. The pressure, p_i is only a function of r, so that we may write $p_1(r) = p_2(r) = p(r)$. Therefore, integrating equation 3 yields two parabolic flow profiles :

$$u_i(r,z) = \frac{1}{2\mu_i} \frac{dp(r)}{dr} \left(z^2 + A_i(r)z + B_i(r) \right), \tag{4}$$

where the functions A_i and B_i are determined by the boundary conditions. These conditions are the non-slip conditions at the ground, $u_2(r,0) = 0$, and at the sphere surface, $u_1(r, h+e)$ $= 0$, the continuity of the velocity at the interface between the two layers, $u_1(r,e) = u_2(r,e)$, and the continuity of the viscous stresses at the interface between the two layers :

$$\mu_1 \frac{\partial u_1}{\partial z}(r,e) = \mu_2 \frac{\partial u_2}{\partial z}(r,e). \tag{5}$$

Solving for the boundary conditions yields

$$B_2(r) = 0, \tag{6}$$

12

$$A_1(r) = A_2(r) = -\frac{(h+e)^2 + (1/k - 1)e^2}{(h+e) + (1/k - 1)e}, \tag{7}$$

$$B_1(r) = -(h+e)A_1(r) - (h+e)^2, \tag{8}$$

where $h \equiv h(r)$. Mass conservation yields

$$q(r) + \pi r^2 w(z = h_0) = 0, \tag{9}$$

where the curvature of the sphere has been neglected. The no-slip condition for the velocity component in z direction yields $w(z = h_0) = -V_0$. The radial flow rate $q(r)$ through a cylinder centered on the axis, of radius r and of height $e + h(r)$, is obtained by integrating the flow fields across the gap as follows

$$q(r) = \int_e^{h+e} u_1(r, z) 2\pi r dz + \int_0^e u_2(r, z) 2\pi r dz. \tag{10}$$

Finally, we find the expression of the radial pressure gradient

$$\frac{dp(r)}{dr} = -\frac{6\mu r V_0}{\bar{h}(r)^3}, \tag{11}$$

where :

$$\bar{h}(r)^3 = 2[e^3(1 - 1/k) - (h + e)^3] + 3A_1(r)[e^2(1 - 1/k) - (h + e)^2] - 6B_1(r)h \tag{12}$$

Note that, for $e = 0$ and $k = 1$, we recover the classical result for one layer : $\bar{h}(r) = h(r)$. The pressure field is obtained by integration of equation 11 between the current radial position, r, and the position $R_0 = \sqrt{2ah_0}$, where it recovers its value at infinity ($p = p_0$ as $r \to \infty$)

$$p(r) - p_0 = \int_r^{R_0} -\frac{dp(r')}{dr'} dr'. \tag{13}$$

A second integration yields the drag force F_B on the sphere

$$F_B = \int_0^a (p(r) - p_0) 2\pi r dr. \tag{14}$$

The integrations are performed numerically with Matlab, for different values of nominal distance, h_0. In contrast to the experiments, the numerical calculation is operated at a given velocity, V_0, thus yielding a different drag for each distance. Hence, the corresponding mobility coefficient $1/f_B$ is obtained by

$$\frac{1}{f_B(\epsilon_0)} = \frac{V(h_0)}{V_{St}} = \frac{6\pi\mu a V_0}{F_B(h_0)} \tag{15}$$

Note that, in equation 15, the function $1/f_B(\epsilon_0)$ depends implicitly on the values of e and k through equation 12. We have checked that, for $e = 0$ and $k = 1$, we recover numerically the classical mobility coefficient $1/f_T$, as illustrated in Figures 6 and 7.

B. Comparison with measurements : Determination of the viscosity coefficient

In the previous section we have demonstrated that the mobility $1/f_B$ of a sphere moving towards a plane interface between two fluids of different viscosities can be calculated in the lubrication approximation. Here, we test the applicability of this model to the mobility of the sphere measured near a textured wall. For this purpose, the height of the bottom layer is set equal to the height of the pillars, e, which is prescribed by the design of the texture and measured by profilometry. The viscosity coefficient, k, is a priori unknown, and has to be obtained by adjustment of the calculated mobility to the experimental curves.

In Figure 6(a), the values of viscosity coefficient, k, have been obtained by the best adjustment of equation 15 (dashed lines) to the mobility curves measured near arrays of cylindrical micro-pillars. Here, the arrays have the same pillar height ($e = 50$ μm), comparable pillar diameters ($2b$ ranges from 40 to 50 μm), but different pillar concentrations ($\phi = 0.1$, 0.2 and 0.3). An excellent agreement is obtained between model and experiments in the region $b/a < \epsilon_0$. Interestingly, the model accurately describes the non-linearity of the mobility curves in that region. Note that the equivalent plane boundary model would simply shift the linear reference curve obtained for a smooth surface. Moreover, the values of k are found to be larger for larger pillar concentrations (5.5, 12 and 28 respectively), consistently with an effective viscosity increasing with pillar concentration.

However, equation 15 does not describe either the rapid deceleration of the sphere just before contacting the top of the pillars ($0 < \epsilon_0 < b/a$), nor the vanishing velocity at contact. Instead, it predicts a non-zero value of velocity at $\epsilon_0 = 0$. To improve this, we choose to model the interaction of the sphere with the closest pillar as follows. Using the pressure field arising from the lubricated squeeze flow between a sphere of radius a and a plane, $p(r) - p_0 = 3\mu a V(h_0)/h(r)^2$, and summing up the resulting normal forces on the surface of a disk of radius b, gives rise to the lubrication drag : $F_P = 6\pi\mu V(h_0)b^2/[2h_0 h(b)]$, and thus to the following mobility coefficient

$$1/f_P(\epsilon_0) = \epsilon_0 \left(1 + 2\,\frac{a^2}{b^2}\,\epsilon_0 \right). \tag{16}$$

Thus, adding the contribution F_P to the drag F_B calculated in section III, we obtain the
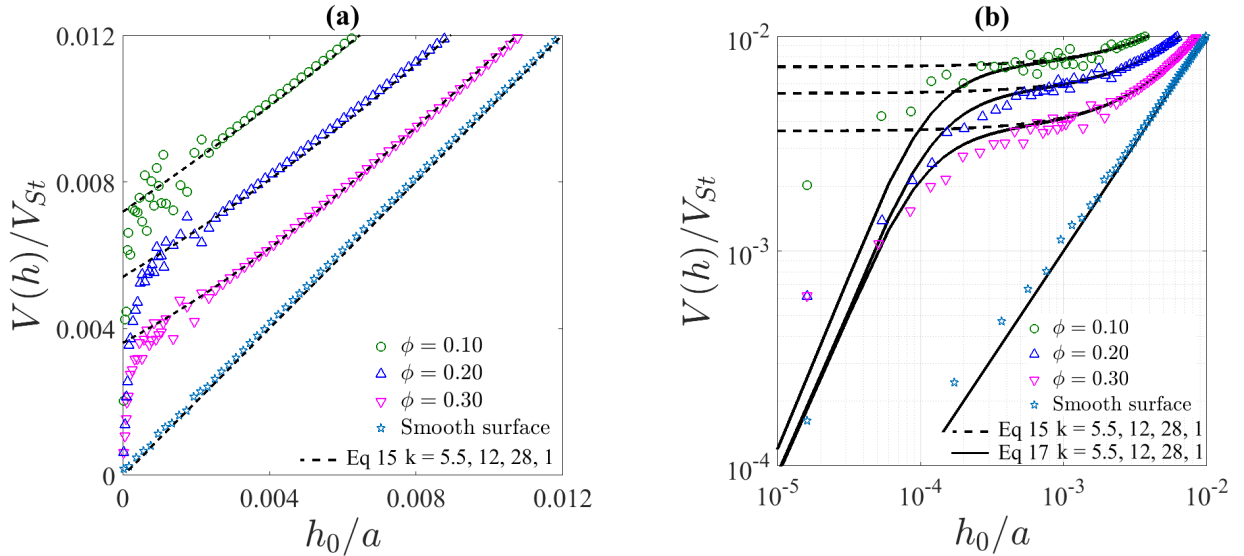
FIG. 6. Symbols : mobility of a sphere of diameter $2a = 7$ mm measured near arrays of cylindrical micro-pillars with $e = 50$ μm and different pillar concentrations $\phi = 0.1, 0.2, 0.3$. The values of b are 20, 25, and 25 μm, respectively. Dashed lines : Equation 15 for $k = 28$, 12, and 5.5 ($k = 1$ for a smooth surface). Continuous lines : Equation 17 for the same values of k. (a) Linear scale (b) Log-Log scale.

sphere mobility in the whole region (iii)

$$\frac{V(h_0)}{V_{St}} = \frac{1}{f_B(\epsilon_0) + f_P(\epsilon_0)}. \tag{17}$$

In Figure 6(b), equations 15 (dashed lines) and 17 (continuous lines) have been plotted with the same values of k. The two equations give identical results in the region $b/a <$ ϵ_0. However, using equation 17, the final sphere deceleration in the region $\epsilon_0 < b/a$ is described correctly, without additional parameter, and with a precision that is sufficient for our purposes. Note that the second term in equation 16 improves over the first term alone : it gives a larger mobility near a small pillar than near a plane. In the following, the parameter k will be searched by adjusting the mobility curves to equation 17.

In Figure 7(a) the same texture is used to modify the mobility of spheres of different diameters (7 and 12.7 mm, respectively). Note that different sphere diameters give rise to different mobility curves when plotted as a function of dimensionless gap h_0/a, a consequence of the textures introducing new length scales, in addition to the sphere diameter[12]. Figure 7(a) depicts also the calculated mobility obtained by the best adjustment of the
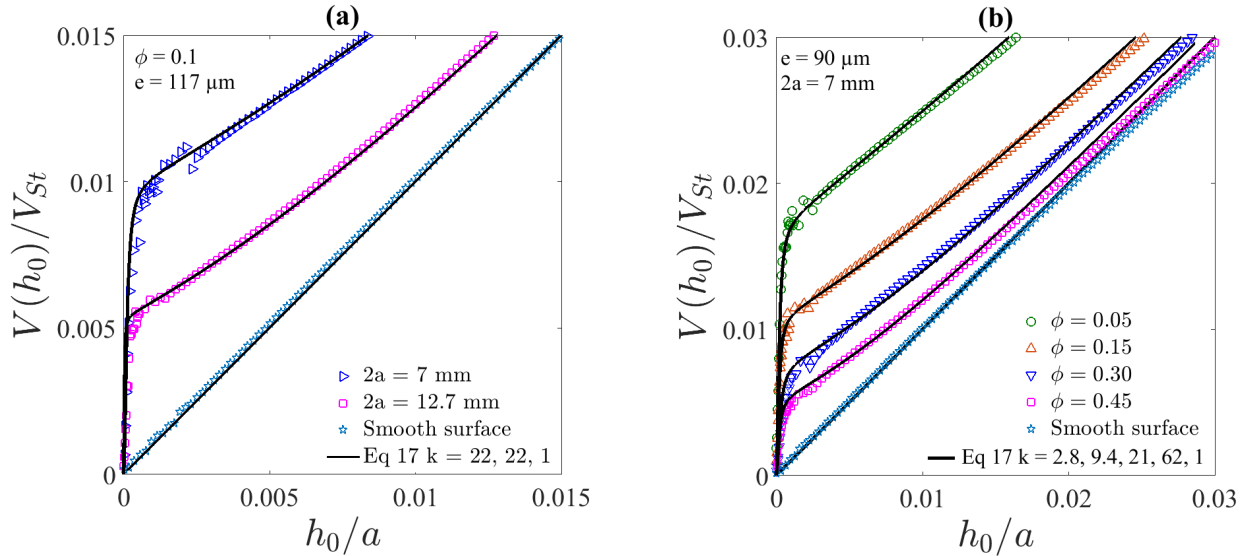
15

FIG. 7. (a) Symbols : mobility measurements of two spheres (diameter $2a = 7$ mm and 12.7 mm) near the same array of cylindrical micro-pillars ($\phi = 0.1$, $e = 117$ μm, $b = 22$ μm). Continuous lines : equation 17 with $k = 22$ ($k = 1$ for the smooth surface). (b) Symbols : Mobility measurements of a sphere (diameter $2a = 7$mm) near arrays of square micro-pillars with $e = 90$ μm and different pillar concentrations $\phi = 0.05$, 0.15, 0.3, and 0.45 ($b = 28$, 30, 53 and 50 μm respectively). Continuous lines : equation 17 with $k = 2.8$, 9.4, 21, and 62 ($k = 1$ for a smooth surface).

model (equation 17) to the experiments. A perfect agreement between the model and the measurements is obtained for the two sphere diameters, yielding a unique value of $k = 22$ for this texture. This supports the idea that the parameter k is a characteristic of the texture geometry. We confirm that this is indeed the case for the range of geometries considered in this work. Only for one of the textures with the highest pillar height ($e = 117$ μm) and high pillar concentration ($\phi = 0.2$), values of k decreasing with increasing sphere diameter have been obtained. We proceeded similarly for arrays of square micro-pillars (in that case the ultimate lubrication interaction of the sphere with one square pillar of side $2b$ is modelled by the interaction between a sphere and a disc of area πb^2, as given by equation 16), and obtained again a very good agreement between model and experiments, as shown in Figure 7(b).

Examining the limitations of the model, it is clear from Figure 7(b) that, in general, the model starts to deviate from the experimental curves at distances ϵ_0 between 0.01 and 0.015. As mentioned earlier, the range of applicability of the model in terms of gap thickness is

restricted to the lubrication region $(h_0 + e) \ll a$. In addition, it is important to note that the present analysis is expected to be limited also in terms of geometrical parameters of the micro-pillar array. Indeed, the saturation of the sphere mobility observed when e/L increases at a fixed concentration ϕ (see Figure 4(b)), supports the idea that when e/L is increased beyond a threshold (which remains to be determined for each value of ϕ), the flow does not penetrate all the way to the bottom of pillars. In that case, our representation of the micro-pillar region by the lubricated squeeze flow of an effective fluid layer extending from $z = 0$ to $z = e$, as depicted in figure 5, does not hold.

At this point, it would be interesting to know if the coefficient k measured here, by adjustment of the model to the data, can be related to the actual viscous dissipation of the flow through the micro-pillar array. Then, it would be possible to correlate k to the geometrical parameters of the micro-pillar array. This point will be discussed in the next section.

IV.   VISCOUS DISSIPATION THROUGH A SQUARE ARRAY OF CYLINDERS

In this section, our aim is to provide a correlation between the value of the viscosity coefficient k obtained in the squeeze-flow experiments, and the geometrical parameters of the textured surface.

A.   Parallel flow

The recent development of flows near micro-textured boundaries has motivated a quantitative understanding of the viscous dissipation through micro-pillar arrays, and hence, a renewed interest for the solutions of the Stokes equations for the flow through arrays of cylinders (see[18] and references therein). Recently, these solutions have been used to predict the effective slip length over superhydrophobic surfaces[19], the coating flow over arrays of micro-pillars[14], and the pressure drop through arrays of cylindrical micro-reactors and micro-heat exchangers[20,21]. In the case of a uniform and unidirectional flow of velocity U, and in the limit of small Reynolds number flows, the drag force per unit length on a single infinite cylinder in a square array is proportional to U, the flow velocity, and to μ, the fluid

viscosity[18]

$$f_p = \beta(\phi)\mu U, \tag{18}$$

where the dimensionless coefficient $\beta(\phi)$ accounts for the hydrodynamic interactions between the cylinders in the array, and is an increasing function of cylinder volume fraction ϕ. Note that $\beta(\phi)$ is independent of the orientation of the flow with respect to the axis of the array, a consequence of the linearity of Stokes equations[22]. The function $\beta(\phi)$ has been determined theoretically in the two limiting cases of dilute and concentrated array (for a detailed review and comparison of the solutions, see reference[20]). Recall that, in the case of a parallel flow over a plane surface covered with a square array of cylindrical pillars of finite height, the viscous dissipation can be evaluated[14,23] by considering a cell of side L, the periodicity of the array, embedding a pillar of height e. In an effective medium approach, the effective viscosity μ_e is defined[14] by adding the viscous force on the bottom wall surface of the cell, F_0, and the drag over the pillar, F_1

$$F_0 + F_1 = \mu_e \langle \dot{\gamma} \rangle L^2, \tag{19}$$

where $\langle \dot{\gamma} \rangle$ is an effective shear rate in the cell. Substituting U by $\langle \dot{\gamma} \rangle z$ in equation 18, and integrating along pillar height, e, yields the drag on a pillar

$$F_1 = \int_0^e f_p \mathrm{d}z = \beta(\phi)\mu\langle \dot{\gamma} \rangle \frac{e^2}{2}. \tag{20}$$

The viscous force exerted by the flow on the bottom wall is

$$F_0 = \mu\langle \dot{\gamma} \rangle L^2. \tag{21}$$

Combining the above equations yields the expression of effective viscosity μ_e as a function of the geometrical parameters of the pillar array

$$\mu_e = \mu \left(1 + c\ \beta(\phi)\frac{e^2}{L^2} \right), \tag{22}$$

where c is a numerical factor equal to $1/2$.

B. Three-dimensional squeeze-flow

In the case of the squeeze flow between a sphere and a wall, which is considered here, the flow through the array of pillars is complicated. Firstly, due to the velocity boundary
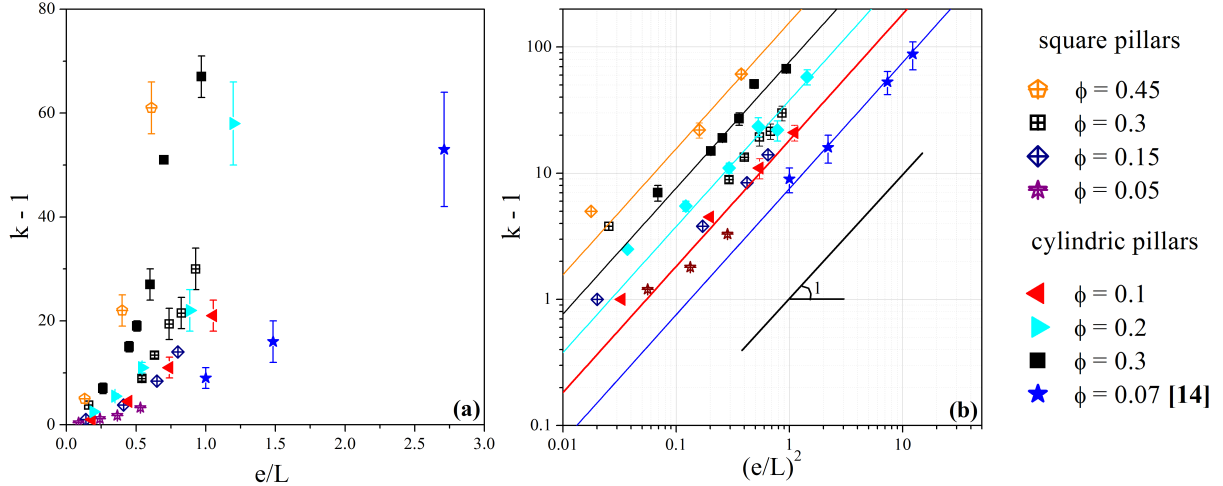
FIG. 8. Reduced effective viscosity, $k - 1$, obtained by adjusting the model developed in section III to the experiments, for various texture geometries, as a function of (a) e/L, (b) $(e/L)^2$. Each symbols refers to a different value of pillar concentration ϕ.

conditions at the top and base of the pillars, the flow is non-uniform along a pillar's height. Secondly, it is the sum of a simple shear-flow and of a pressure driven flow. However, both effects could be handled analytically by integrating the flow along a pillar's height. Another complication arises from the radial geometry of the squeeze flow above the pillars. To our knowledge, there exists no predictions for the viscous dissipation by a flow forced radially through a square array of pillars. The absence of rotational symmetry in the pillar array may introduce some anisotropy, particularly at large pillar concentrations. This flow could be solved numerically, however such a study is beyond the scope of the present work.

Here, we carry out a simple comparison between the effective viscosity measured in this work, $k\mu$, to the effective viscosity that would be obtained for a parallel flow through the same micro-pillar array (equation 22). The values of the factor k extracted from our experiments using arrays of cylindrical or square pillars with different geometrical parameters (e, L and b) are summarized in Figure 8. The error bars are based on the quality of the adjustment, which deteriorates only, as already mentioned, for the highest values of pillar's concentrations and heights.

In Figure 8(a) the reduced viscosity ($k - 1$) is plotted as a function of e/L. Each symbol refers to a set of data obtained for the same pillar concentrations ϕ. Clearly, the effective viscosity increases with the pillar concentration and with the ratio e/L. In Figure 8(b),

19

$(k-1)$ is plotted as a function of $(e/L)^2$, in Log-Log scale. The data obtained for a given value of pillar concentration collapses onto a straight line, of slope equal to 1, showing that the scaling predicted by equation 22 applies also in the case of a radial flow. The continuous lines in Figure 8(b) are obtained by linear regression, and provide a ratio $(k-1)/(e/L)^2$ for each value of ϕ, denoted as $B(\phi)$, and displayed in Table 1.

Figure 8(b) shows that, in the range of parameter tested here ($e/L \leq 1.5$ and $\phi \leq 0.45$), the scaling behavior $(k-1) \backsim (e/L)^2$ still holds for a radial flow. This can be understood as follows. We consider an array of micro-pillars with a given geometry. In contrast to a parallel flow, the effective viscosity is here spatially varying, as its value in individual cells containing one pillar depends on the geometry of the flow in that cell. The measured effective viscosity thus amounts to an averaging of the contribution to viscous dissipation of the different cells. In a rudimentary description, we consider that the cells situated at the same distance r from the center of the radial flow have the same contribution, and that the viscous force on the bottom surface, F_0, and the drag force on the pillar, F_1, are functions of the distance r only. For a given cell, they may be written as

$$F_0(r) = \mu \bar{\dot{\gamma}}(r) L^2, \qquad F_1(r) = \mu \beta(r) \bar{\dot{\gamma}}(r) \frac{e^2}{2}, \qquad (23)$$

where $\beta(r)$ is a dimensionless friction coefficient, yielding the drag per unit length on the pillar, $\beta(r)\mu U$, and $\bar{\dot{\gamma}}(r)$ is an effective shear rate. We define an averaged effective viscosity μ_e^* by integrating the viscous forces in the different cells over a disk of radius R which is large compared to L

$$\mu_e^* \langle \dot{\gamma}_R \rangle \pi R^2 = \frac{1}{L^2} \int_0^R (F_0(r) + F_1(r)) 2\pi r \mathrm{d}r, \qquad (24)$$

where $1/L^2$ is the number density of cells. In equation 24, $\langle \dot{\gamma}_R \rangle$ is the average of the effective shear rates, defined as

$$\langle \dot{\gamma}_R \rangle = \frac{1}{\pi R^2} \int_0^R \bar{\dot{\gamma}}(r) 2\pi r \mathrm{d}r. \qquad (25)$$

Combining the above equations leads to the expression of the averaged effective viscosity μ_e^*

$$\mu_e^* = \mu \left(1 + 0.5 \, \bar{\beta}(R) \frac{e^2}{L^2} \right), \qquad (26)$$

where $\bar{\beta}(R)$ is an average of the friction coefficients

$$\bar{\beta}(R) = \frac{\int_0^R \beta(r) \bar{\dot{\gamma}}(r) 2\pi r \mathrm{d}r}{\langle \dot{\gamma}_R \rangle \pi R^2}. \qquad (27)$$

Note that a cell situated at a distance r, is subjected to a diverging flow whose angle of aperture is $\approx L/r$. This angle decreases as r increases, and becomes negligibly small when r is sufficiently large compared to L. In that case, the flow in the cell can be considered as unidirectional, and the friction coefficient $\beta(r)$ becomes independent on r and equal to $\beta(\phi)$ defined in equation 18. Experimentally, the fact that the measured effective viscosity is independent of the sphere diameter is consistent with an average friction coefficient $\bar{\beta}(R)$ becoming a constant for sufficiently large values of R.

Finally, we discuss the values of $B(\phi)$ obtained from linear regression in Figure 8. For a parallel flow through the same pillar array, equation 22 predicts that $B(\phi)$ would be equal to $0.5\beta(\phi)$. For comparison purposes, we use here an analytical solution[24], that is valid up to a concentration of $\phi = 0.4$ and provides a good agreement with numerical and experimental data[18]

$$\beta(\phi) = \frac{4\pi}{ln(\frac{1}{\sqrt{\phi}}) - 0.75 + \phi - \frac{1}{4}\phi^2}. \tag{28}$$

We have reported in Table 1 the values of $\beta(\phi)$ predicted by equation 28. The ratio $B(\phi)/\beta(\phi)$ measured in our experiments and in the coating flow experiments[14] is reported in the last column of Table 1. Note that the coating flow gives rise to a ratio of 0.37, which may be a consequence of the flow profile along a pillar's height (we used a simple shear flow for deriving equation 22). In our experiments, a narrow range of values of the ratio $B(\phi)/\beta(\phi)$, of the order of 0.75 (between 0.74 and 0.85), are obtained for the arrays of cylindrical pillars, indicating a correlation between the measurements for a radial flow and the predictions for a parallel flow through the micro-pillar array. Hence, the radial flow gives rise to a larger dissipation than the parallel flow. For the arrays of square pillars, the ratio $B(\phi)/\beta(\phi)$ remains of the same order of magnitude as for the cylindrical pillars, but for the smaller pillar concentrations only. For larger concentrations, the values of the ratio are more scattered. We eventually conclude that in the range of parameters explored here, the averaged effective viscosity measured in our experiments is reasonably correlated to the geometrical parameters of the micro-pillar array, using equation 22, with a prefactor c that is of the order of 0.75 (instead of 0.5 for a parallel flow and 0.37 for a coating flow).

	ϕ	$B(\phi) = (k-1)/(e/L)^2$ from Fig. 8	$\beta(\phi)$ from Eq. 28	$B(\phi)/\beta(\phi)$
Cylindrical pillars	0.1	18.3	24.8	0.74
	0.2	38.2	50.8	0.75
	0.3	76.4	90.3	0.85
Square pillars	0.05	10	13.8	0.72
	0.15	20.3	36.2	0.56
	0.3	31.2	90.3	0.35
	0.45	158.6	107	1.48
Coating flow[14]	0.07	7.2	19.4	0.37

TABLE I. Comparison between the reduce effective viscosity, $(k-1)/(e/L)^2$, measured from experiments with a radial flow through the pillar array (Figure 8.b), and the prediction by equation 28 for a parallel flow through the same array of pillars. Also shown is the experimental result for a coating flow through an array of cylindrical pillars[14].

V. CONCLUSION

We have reported on measurements of the dynamics of a millimetric sphere settling in a viscous fluid towards a wall decorated with an array of micro-pillars. The focus is on the near-field region, where the gap between the sphere and the top of pillars is of the order of, or smaller than, the periodicity of the pillar array. We have varied the geometrical parameters of the texture, i.e. the height and diameter (resp. the side length) of the cylindrical (resp. square) pillars, and the periodicity of the array. As a result of the fluid drainage through the array of pillars, the velocity of the sphere at a given distance from the top of the pillars is larger than when measured at the same distance from a plain smooth wall. To reproduce this velocity enhancement, we have developed a squeeze flow model of two adjacent fluid layers, one of these layers having an effective viscosity larger than the viscosity of the bulk fluid, thus taking into account the viscous dissipation of the flow through the array of pillars. In the range of geometries tested in this work, the model describes very precisely the velocity-distance curves, with an effective viscosity which can be correlated to the geometrical parameters of the textures.

ACKNOWLEDGMENTS

REFERENCES

[1] H. Brenner, "The slow motion of a sphere through a viscous fluid towards a plane surface," Chem. Eng. Sci. **16**, 242–251 (1961).

[2] A. D. Maude, "End effects in a falling-sphere viscometer," British J. of Appl. Physics **12**, 293–295 (1961).

[3] J. R. Smart and D. T. Leighton, "Measurement of the hydrodynamic surface roughness of noncolloidal spheres," Phys. Fluid A **1**, 52–60 (1989).

[4] N. Lecoq, R. Anthore, B. Cichocki, P. Szymczak, and F. Feuillebois, "Drag force on a sphere moving towards a corrugated wall," J. Fluid Mech. **513**, 247–264 (2004).

[5] R. H. Davis, Y. Zhao, K. P. Galvin, and H. J. Wilson, "Solid-solid contacts due to surface roughness and their effect on suspension behaviour," Phil. Trans. R. Soc. Lond. A **361**, 871–894 (2003).

[6] G. Z. Ramon, H. E. Huppert, J. R. Lister, and H. A. Stone, "On the hydrodynamic interaction between a particle and a permeable surface," Phys. Fluids **25**, 073103 (2013).

[7] A. Steinberger, C. Cottin-Bizonne, P. Kleinmann, and E. Charlaix, "High friction on a bubble mattress," Nature materials **6**, 665–668 (2007).

[8] A. Maali, Y. Pan, B. Bushnan, and E. Charlaix, "Hydrodynamic drag-force measurement and slip length on microstructured surfaces," Phys. Rev. E. **85**, 066310 (2012).

[9] O. Vinogradova and G. Yakubov, "Surface roughness and hydrodynamic boundary conditions," Phys. Rev. E **73**, 045302 (2006).

[10] R. Gupta and J. Fréchette, "Measurement and scaling of hydrodynamic interactions in the presence of draining channels," Langmuir **28**, 14703–14712 (2012).

[11] N. Lecoq, "Boundary conditions for creeping flow along periodic or random rough surfaces : experimental and theoretical results," Journal of Physics : Conference Series **392**, 012010 (2012).

[12] A. Mongruel, T. Chastel, E. S. Asmolov, and O. I. Vinogradova, "Effective hydrodynamic boundary conditions for microtextured surfaces," Phys. Rev. E **87**, 011002(R) (2013).

[13] E. Asmolov, A. Belyaev, and O. Vinogradova, "Drag force on a sphere moving toward an anisotropic superhydrophobic plane," Phys. Rev. E **84**, 026330 (2011).

[14] J. Seiwert, C. Clanet, and D. Quéré, "Coating of a textured solid," J. Fluid Mech. **669**, 55–63 (2011).

[15] N. Lecoq, F. Feuillebois, N. Anthore, R. Anthore, F. Bostel, and C. Petipas, "Precise measurement of particle-wall interactions at low Reynolds number using laser interferometry," Physics of fluids A **5**, 3–12 (1993).

[16] R. G. Cox and H. Brenner, "The slow motion of a sphere through a viscous fluid towards a plane surface - II Small gaps widths, including inertial effects," Chem. Eng. Sci **22**, 1753–1777 (1967).

[17] M. O'Neill and K. Ranger, "The approach of a sphere to an interface," Phys. Fluids **26**, 2035–2042 (1983).

[18] J. E. Drummond and M. I. Tahir, "Laminar viscous flow through regular arrays of parallel solid cylinders," Int. J. Multiphase Flow **10**, 515–540 (1984).

[19] C. Ybert, C. Barentin, C. Cottin-Bizone, P. Joseph, and L. Boquet, "Achieving large slip with superhydrophobic surfaces : scaling laws for generic geometries," Phys. Fluids **19**, 123601 (2007).

[20] J. Yeom, D. D. Agonafer, J. H. Han, and M. A. Shannon, "Low Reynolds number flow across an array of cylindrical microposts in a microchannel and figure-of-merit analysis of micropost-filled microreactors," J. Micromech. Microeng. **19**, 065025 (2009).

[21] R. Xiao, R. Enright, and E. N. Wang, "Prediction and optimization of liquid propagation in micropillar array," Langmuir **26**, 15070–15075 (2010).

[22] D. L. Koch and A. J. C. Ladd, "Moderate Reynolds number flows through periodic and random arrays of aligned cylinders," J. Fluid Mech. **349**, 31–66 (1997).

[23] C. Ishino, M. Reyssat, E. Reyssat, K. Okumura, and D. Quéré, "Wicking within forests of micropillars," Europhys. Lett. **79**, 56005 (2007).

[24] S. Kuwabara, "The forces experienced by randomly distributed parallel cylinders perpendicular to the flow direction at small Reynolds number," J. Phys. Soc. Japan. **14**, 527–532 (1959).